Determination of small soot particles in the presence of large ones from time-resolved laser-induced incandescence

E. Cenker · G. Bruneaux · T. Dreier · C. Schulz

Abstract A novel strategy for the analysis of time-resolved laser-induced incandescence (TiRe-LII), called two-exponential reverse fitting (TERF), is introduced. The method is based on combined monoexponential fits to the LII signal decay at various delay times and approximates the particle-size distribution as a weighted combination of one large and one small monodisperse equivalent mean particle size without requiring assumption on the particle-size distribution. The effects of particle size, heat-up temperature, aggregate size, and pressure on the uncertainty of this method are evaluated using numerical experiments for lognormal and bimodal size distributions. TERF is applied to TiRe-LII measured in an atmospheric pressure laminar non-premixed ethylene/air flame at various heights above burner. The results are compared to transmission electron microscopy (TEM) measurements of thermophoretically sampled soot. The particle size of the large particle-size class agreed well for both methods. The size of the small particle-size class and the relative contribution did not agree which is attributed to missing information in the TEM results for very small particles. These limitations of TEM measurements are discussed and the effect of the exposure time of the sampling grid is evaluated.

1 Introduction

Emission of particulate matter (PM) in combustion processes is a major issue due to its negative impacts on human health and world climate. It is therefore of great interest to understand soot formation processes well enough that new concepts can be developed that help limit these emissions. Powerful diagnostics tools are required that measure the properties of soot in various environments. The primary soot particle diameter d_p is one key indicator for interpreting the effects of soot formation and burnout. Soot usually has polydisperse size distributions, and small and large particles show a distinctly different behavior in terms of transport and reactivity. Information about the size distribution is therefore important for a better understanding of soot formation and oxidation.

Time-resolved laser-induced incandescence (TiRe-LII) is an optical in situ technique for measuring the particle size [1]. Soot particles are heated via absorption of light from a laser pulse to temperatures above 3,000 K, and the subsequent blackbody radiation is recorded during the cooling phase. In a zeroth-order approximation, the signal shows an exponential decay after the laser pulse and small particles cool down faster than large ones due to their larger surface-to-volume ratio. Quantitative particle-size information can be obtained from a best-fit comparison of the temporal signal decay and simulations based on the particle's energy- and mass-balance equations [2–4].

E. Cenker · G. Bruneaux
IFP Energies Nouvelles, Institut Carnot IFPEN Transports Energie, 1 et 4 avenue de Bois-Préau, 92852 Rueil-Malmaison, France

G. Bruneaux
e-mail: gilles.bruneaux@ifpen.fr

E. Cenker · G. Bruneaux
École Centrale Paris, Chatenay-Malabry, France

E. Cenker (✉) · T. Dreier · C. Schulz
Institute for Combustion and Gas Dynamics – Reactive Fluids (IVG) and Center for Nanointegration Duisburg-Essen (CENIDE), University of Duisburg-Essen, Duisburg, Germany
e-mail: emre.cenker@uni-due.de
e-mail: thomas.dreier@uni-due.de

C. Schulz
e-mail: christof.schulz@uni-due.de

Regardless of the actual particle-size distribution, a direct fitting for the entire signal trace with a single-exponential function yields a monodisperse equivalent mean particle size that is known to be biased toward larger sizes for polydisperse ensembles [5]. By assuming a size distribution, more complex decay curves are generated and information about the particle-size distribution (its shape and its mean value) can be gained from TiRe-LII. Lognormal size distributions are good approximations for various flame conditions and are widely assumed for data evaluation [2, 6–8]. Nevertheless, it is generally challenging to fit polydisperse distributions to LII signal decays because the fitting problem is ill-posed [9]. Particle-size distributions with various combinations of count median diameter d_{cmd} and geometric standard deviation σ_{g} might therefore produce almost identical simulated LII signal decay profiles, and therefore, the evaluation of the measured data does not always lead to unique solutions. Additionally, a lognormal size distribution may not always be the best assumption. It is reported that multi-lognormal [10] or bimodal distributions [11, 12] may show better agreement for some specific environments.

An alternative approach takes advantage of the fact that the various size classes contribute to the LII signal decay curve in a different way depending on the delay after laser heating. While the early decay is strongly influenced by the small particle fraction, the late signal is dominated by signal from large particles. Rather than fitting a multi-parameter function to the entire (mostly featureless) decay and minimizing the fitting error over the full curve, we split the problem in the time domain. In each temporal subsection, the mathematical form of the decay curves can be simplified and the fitting problem becomes better defined (less ill-posed). Dankers et al. [13] showed a rather simple engineering approach that determines d_{cmd} and σ_{g} from exponential fits to the LII signal decay at two different delay times and within predetermined time intervals. Nevertheless, this method is also based on pre-assumed lognormal distributions.

In this paper, a new strategy is presented for determining particle-size information from TiRe-LII. We call this signal evaluation concept two-exponential reverse fitting (TERF). The method shows some similarity to Dankers et al. [13] because it also uses a single-exponential fit for a delayed part of the LII-signal trace, but in contrast, it does not require to pre-assume a particle-size distribution. The TERF method differentiates between signal contributions from small and large particles. It determines monodisperse equivalent mean particle sizes for both size groups and evaluates the relative ratio of particle number densities for both groups.

The evaluation is based on a simplifying exponential approximation. To verify its applicability, its variation from a simulated ideal LII-signal trace is evaluated by using least-squares fitting. The influence of various experimental conditions on this approximation, such as heat-up temperature, pressure, particle size, and aggregate size, is quantitatively investigated. The novel particle-sizing method is tested on phantom signals that were simulated for well-defined conditions and particle-size distributions. Finally, the method is applied to experimental LII data acquired in a co-annular laminar non-premixed ethylene/air flame at various heights above the burner (HAB). The results are compared to transmission electron microscopy (TEM) measurements of thermophoretically sampled soot at the same locations.

2 Theory

The methodology for TiRe-LII particle sizing is described, e.g., in [3]. In the present work, we use the original code for LIISim [4] imbedded in MATLAB routines and details of all routines in this tool are presented, e.g., in [7]. For atmospheric conditions, considerable evaporation starts at around 3,400 K [6] and becomes stronger with increasing temperature. The present modeling and experimental study is aimed at avoiding these complications by keeping laser fluences below levels where significant evaporation takes place, i.e., keeping the maximum heat-up temperature below the vaporization threshold. In all simulations, the particles were assumed to be graphite like using the respective materials properties [11]. The aggregate size within a probe volume is assumed to be uniform in this work. For heat conduction, the Fuchs approach [14] is chosen in LIISim that is known as the most appropriate model for particle–gas energy exchange in a wide range of gas pressures [15].

2.1 Polydispersity

The TiRe-LII signal acquired from polydisperse soot is the superposition of individual decaying functions for the various size classes weighted by their respective probability df. For a lognormal distribution, df of a particle size class between d_{p} and $d_{\mathrm{p}} + dd_{\mathrm{p}}$ is

$$df = \frac{1}{\sqrt{2\pi} d_{\mathrm{p}} \ln \sigma_{\mathrm{g}}} \exp \left[-\frac{\left(\ln d_{\mathrm{p}} - \ln d_{\mathrm{cmd}} \right)^2}{2 \left(\ln \sigma_{\mathrm{g}} \right)^2} \right] dd_{\mathrm{p}} \qquad (1)$$

Evaluating the particle size from such a signal with a monodisperse assumption yields a monodisperse equivalent mean particle size that is biased toward larger sizes. The magnitude of this bias is related to the width (i.e., σ_{g}) of the distribution. To quantify the bias, a set of LII signals was simulated with a polydisperse (lognormal) particle

**Table 1** Input parameters for modeling the standard "control signal"

Property	Standard condition
Particle-size distribution	Monodisperse
Particle size	30 nm
Aggregate size	50
Ambient pressure	1 bar
Bath gas temperature	1,750 K
Maximum heat-up temperature	3,300 K
Thermal accommodation coefficient	0.25
$E(m)$	0.4
Detection spectral range	410–440 nm
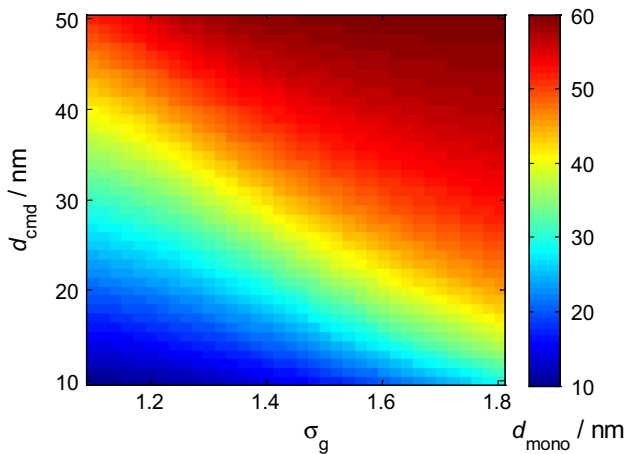
Fig. 1 Monodisperse particle sizes evaluated from synthetic LII signals simulated for lognormal particle-size distributions with various values of d_{cmd} and σ_g

ensemble for d_{cmd} varying from 10 to 50 nm in 1-nm increments and σ_g varying from 1.1 to 1.8 in 0.02 increments. To ensure that each signal trace covers the entire process from reaching the peak temperature back to thermal equilibrium with the bath gas, the duration of each simulation was set to 2 μs. Input parameters are given in Table 1. For
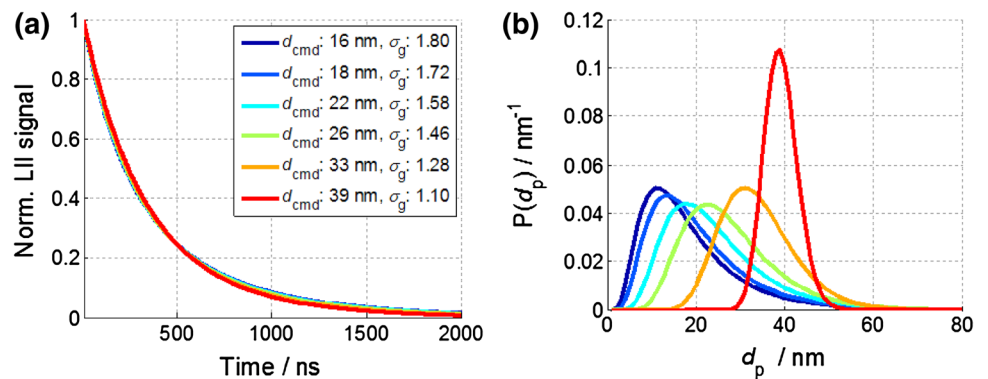
each case, the signal was then evaluated using a monodisperse approach.

The results for the monodisperse response to the polydisperse input are shown in Fig. 1. The determination of the particle-size distribution using an inverse approach is an ill-posed problem. To better illustrate this, six TiRe-LII-signal traces with the same monodisperse equivalent mean particle size of 40.2 nm (same color code in Fig. 1), but differing values of d_{cmd} and σ_g are selected. The almost identical LII-signal traces are plotted on Fig. 2a. Figure 2b shows the strongly varying underlying particle-size distributions with the respective color code (each data point on the distribution curve represents the probability density of a 1-nm-wide bin).

This comparison makes clear that signal interpretation based on standard inversion schemes suffers from this ambiguity with a fairly wide range of satisfactory solutions. To overcome this problem, various approaches were proposed and Daun et al. [16] reviewed various implicit solution schemes for recovering particle-size distributions from TiRe-LII data. It is shown that such implicit solution approaches suffer loss of accuracy when the input data is slightly modified or when the noise contribution to the measured signal is considerable. Furthermore, approaches that aim at solving the forward problem are time intensive, and thus, they are not suitable for on-line analysis.

2.2 Single-exponential approximation

In the absence of strong evaporation, heat conduction is the dominant cooling mechanism of soot particles after laser heating. During this cooling, the decay rate remains almost unchanged for an isolated particle or a soot aggregate composed from monodisperse particles, and therefore, the LII signal can be approximated by a single-exponential decay. Liu et al. [17] presented the temporal variation of the particle temperature of monodisperse soot (for various particle sizes). The signals were simulated for moderate laser fluence and non-premixed atmospheric flame conditions.

Fig. 2 a TiRe-LII signals simulated for soot ensembles with the particle-size distributions shown in (b)
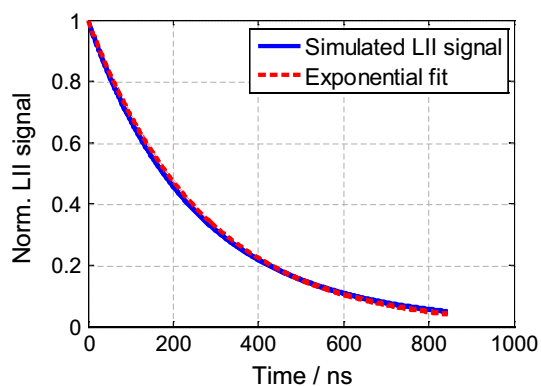
Fig. 3 Simulated LII signal for a monodisperse aggregate (conditions given in Table 1) and a monoexponential fit

For all mean particle sizes, the results exhibit a nearly linear decay in logarithmic diagrams, i.e., the signal decays almost exponentially. A single-exponential decay

$$y = k\mathrm{e}^{-t/\tau} \tag{2}$$

where k is the pre-exponential factor, t is the time, and τ is the lifetime of the LII signal of the respective size group can then be used for the description of the signal decay. To verify the accuracy of this approximation, a "control LII signal" is simulated for the input parameters shown in Table 1 that is later on used as a reference case for comparison with simulated signals with varying input parameters.

An exponential function is fitted to this control signal with a least-squares minimization routine for the time range where the LII-signal intensity decays to 5 % of its peak value. Both curves are shown in Fig. 3.

The goodness of the fit R^2 is over 0.9994. To quantify the systematic error in particle sizing due to such an approximation, LII-signal curve fitting is performed by using the new exponential fit (red dashed curve) and the identical input parameters of the control LII signal as model input. This fitting yielded a particle size of 30.6 nm which is only 2 % larger than the original input. This minor deviation results from the small contributions of radiation and evaporation to the total cooling. Each of these heat exchange mechanisms contributes its own independent exponential decay rate leading to a deviation from the monoexponential decay. Because of the low heat-up temperature in the control case, the difference, however, is negligible.

For the validity of the monoexponential approximation, the experimental conditions (i.e., input parameters of the simulation) are important as they influence the relative importance of the various heat exchange mechanisms. To quantify this influence, the same procedure is repeated by systematically changing one individual input parameter (keeping all others fixed), and the resulting systematic errors (i.e., the difference (in %) between evaluated

particle size when fitting the single-exponential decay with the LII model function and the given size) are shown in Fig. 4 for varying pressure, particle size, aggregate size, and heat-up temperature. Unless otherwise stated, each simulation is performed with the conditions shown in Table 1.

In many practical combustion devices, soot is formed at elevated pressure. At high pressure, the LII-signal lifetime is significantly reduced due to enhanced heat transfer caused by increased collision rates. In comparison, pressure has a negligible effect on the evaporation rate and radiation is not affected at all. Therefore, with increasing pressure, the importance of conduction in the total heat exchange further increases, and the LII signal converges to a single-exponential decay. Figure 4a shows this effect for pressures from 1 to 60 bar in 1 bar increments. The systematic error further reduces from 2 % at 1 bar to below 0.5 % at high pressures. The particle-sizing routine of LIISim has a resolution of 0.1 nm. Therefore, the evaluated systematic error shows distinct steps as a function of pressure.

The systematic error evaluated for particles from 4 to 80 nm with 1-nm increments is shown in Fig. 4b (4 nm is the minimum input value for LIISim). The actual data are shown with black dots, and the curve is a second-order polynomial fit to illustrate the trend. The oscillation of the data is caused by the 0.1-nm resolution of LIISim. Theoretically, no dependence on the error on particle size is expected because all the heat exchange mechanisms are affected equally. Nevertheless, a slight 1 % change in the systematic error is observed over the given particle size range (systematic error starts to reduce after around 40 nm). This is, however, a result of the data format of LIISim. By default, LIISim uses the first microsecond of the data only for fitting. When the particle size increases from 4 to 80 nm, the LII-signal lifetime increases from ~30 ns to ~2 μs (it exceeds 1 μs at around 40 nm). With large particles, a part of the signal trace is thus disregarded. Such a partial using of the LII signal results in a better fitting by a single-exponential function. Therefore, for particles larger than 40 nm, smaller systematic errors are observed. If the curve-fitting routine was not limited in time, no particle diameter dependence would occur.

Soot aggregates can be described as random fractal structures. In LII modeling, the evaporation rate, the change in internal energy, and the heat loss due to radiation are not affected by aggregation as long as the individual particles remain in the Rayleigh regime. The signal scales linearly with the number of primary particles within an aggregate and hence the mass [18]. However, heat conduction is affected by aggregation. A primary soot particle within an aggregate cools down more slowly than an isolated one because of shielding by the surrounding particles [19]. Figure 4c shows the systematic

Fig. 4 Systematic errors in particle sizing due to approximating a simulated LII decay with a monoexponential decay for varying pressure (**a**), particle size (**b**), aggregate size (**c**), and heat-up temperature (**d**)
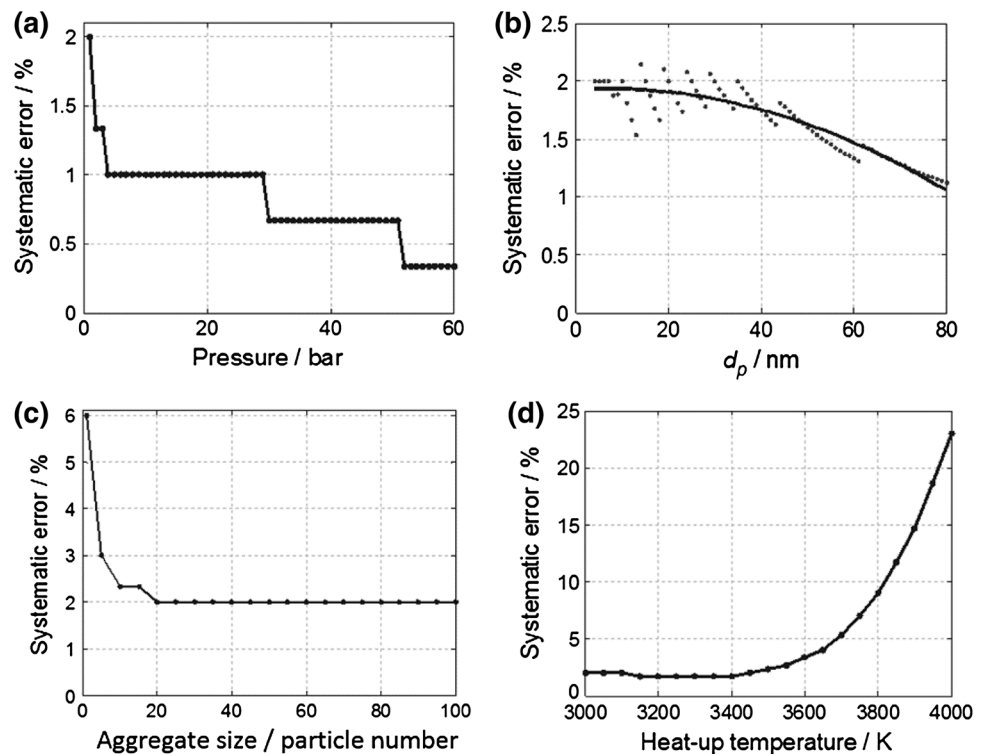
error for an isolated particle and aggregates with 5–100 particles. With increasing aggregate size, the contribution of heat conduction to the total cooling decreases which leads to the assumption of an increasing deviation from a monoexponential decay. Surprisingly, the results show the opposite trend. The greatest change occurs when switching from isolated particles to the aggregate model. For aggregates larger than 20 particles, the magnitude of the change is below the resolution of LIISim. This contradiction requires further investigation and might indicate an incorrect treatment of shielding effects in the underlying submodel in LIISim.

The particle heat-up temperature reached during the laser pulse depends on laser fluence. A change of this parameter influences the heat exchange rates of radiation, conduction, and evaporation. The most critical change occurs with evaporation when the temperature exceeds approximately 3,400 K (Fig. 4d). Its contribution to the total cooling increases significantly which causes a strong deviation from the single-exponential decay.

All these analyses indicate that, compared to other uncertainties in LII particle sizing [20], the error due to the monoexponential approximation is minor for monodisperse particle ensembles heated in the low-fluence regime. Deviating from the low-fluence regime, however, causes a strong deviation from the monoexponential assumption. Increasing pressure in contrast is beneficial. Hence, to benefit from the simplicity of fitting exponential functions, this

approximation can be used as a tool for further detailed size-distribution analysis.

2.3 Size-distribution analysis with the TERF method

In polydisperse particle ensembles where each size group has a unique LII-signal lifetime, the signal superposition causes a deviation from the monoexponential decay behavior. The relative contribution of each size group is linearly proportional to its relative volume fraction f_v. Hence, such a LII signal cannot be accurately approximated by monoexponential decay. Nevertheless, with increasing time after the laser heat up, the particle temperature depends on size. Because smaller particles cool faster than larger ones, their contribution to the overall LII signal decreases over time and the remaining signal becomes increasingly dominated by the larger particles [2].

The TERF method couples the fact that the LII signal is dominated by large particles at long delay times with approximating this part of the signal by a monoexponential decay to derive information about the particle-size distribution. When starting the signal evaluation after a certain delay after laser heat up, the remaining signal trace preferentially represents the largest particles. Although this signal still contains contributions from particles with various particle sizes, the relative size distribution is narrowing with increasing delay. For such narrow distributions, it has been shown [9, 13] that particle sizing via a monodisperse fitting
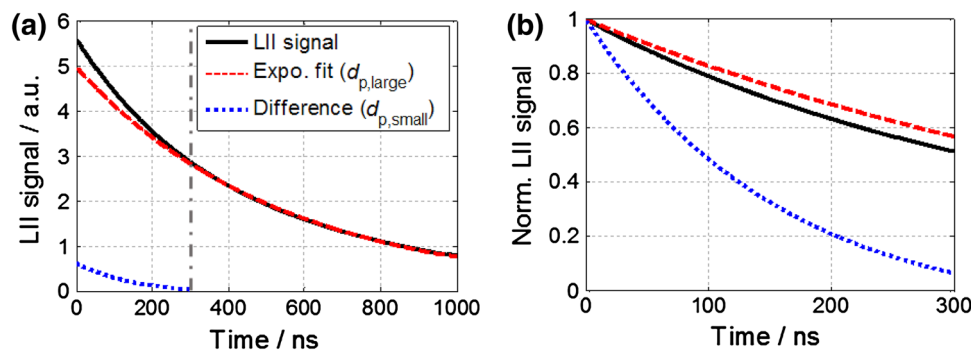
Fig. 5 a Simulated LII signal for polydisperse soot with a lognormal distribution ($d_{cmd} = 20$ nm, $\sigma_g = 1.8$, *black solid line*). A monoexponential decay is fitted to the section of the LII signal from 300 ns down to 5 % of the peak signal and extrapolated back into the time domain from 0 to 300 ns (*red dashed line*). The difference between both *curves* represents the signal contribution from small particles (*blue dotted line*). **b** The same data normalized to the respective peak values

yields a good approximation for the mean particle size. Therefore, monoexponential fitting eventually becomes possible with an acceptable uncertainty that represents the large particles in the ensemble. Once the parameters of the monoexponential fit are determined, the respective signal contribution of the subsection of the particle ensemble can be extrapolated back in time into the time domain before the above-mentioned delay and into the data disregarded before. This extrapolated curve represents the theoretical cooling of the large particle fraction right after the laser pulse and has a slower decay rate than the overall signal. The additional signal (the difference between the measured signal and the back-extrapolated signal) then stems from smaller particles.

The TERF method provides additional improvement to the minimization operation in the nonlinear least-squares problem when compared to full curve fitting. In the conventional approach, the best fitting, hence the particle size, is determined by selecting the curve parameters that yields the closest resemblance to the original signal. When fitting a LII signal from a polydisperse soot ensemble, the governing equation cannot describe the actual physics entirely, and the best fitting is achieved only with local deviations of the model curve from the original signal. For instance, a good fitting of the first 20–30 ns after the laser pulse, where the gradients are very high in the signal, increases the overall goodness of the fitting, and it is automatically preferred by the curve-fitting algorithm. However, such fitting results in considerable deviation of the modeled curve in the delayed part of the signal. This eventually causes inaccurately calculated particle sizes. With TERF, the shortened time domain of the signal provides a better fitting and the local variations between the signal and the modeled curve diminishes.

To illustrate this TERF approach, a LII-signal trace is simulated with a wide lognormal distribution

($d_{cmd} = 20$ nm, $\sigma_g = 1.8$, black curve in Fig. 5a). All the other parameters are those from Table 1. The delay time for starting the data evaluation is 300 ns (dash-dotted gray vertical line), and a monoexponential function is fitted to the delayed signal portion that is then extrapolated back to the 0–300 ns time range (dashed red line). The original LII signal has a steeper decay than that of the back-extrapolated fit, and it is stronger because of the additional contribution of signal from small particles (shown by the blue dotted curve). The comparison of the normalized curves (Fig. 5b) shows the difference in decay times and thus the origin from different subsections of the particle-size ensemble. It should be noted that the signal representing the small particle class (blue dotted line) is also composed of contributions from various particle sizes; however, the distribution is again narrower than that of the total ensemble.

A monodisperse equivalent particle size can be evaluated from each of these LII signals representing small and large particles, respectively. The evaluation of the time-delayed data requires the knowledge of the actual temperature of the particles at that delay as heat-up temperature for the LIISim simulation. When calculating the extrapolated exponential curve starting at 0 ns, the original heat-up temperature can be used and a temporally resolved temperature information is not necessary. In Fig. 6, the evaluated small and large monodisperse equivalent particle sizes, $d_{p,small} = 15$ nm and $d_{p,large} = 57$ nm, are shown along with the actual distribution of the particle size used for the simulation (each data point on the distribution curve represents the probability density of a 1-nm-wide bin). These particle sizes represent a mean of different size classes at the two ends of the distribution curve. When particle sizing is performed with the entire LII signal (from peak signal to 5 % of this peak) using a monodisperse approach, the evaluated particle size is 45.3 nm.

In addition to the mean particle sizes from both size classes, the ratio of their number densities can be evaluated
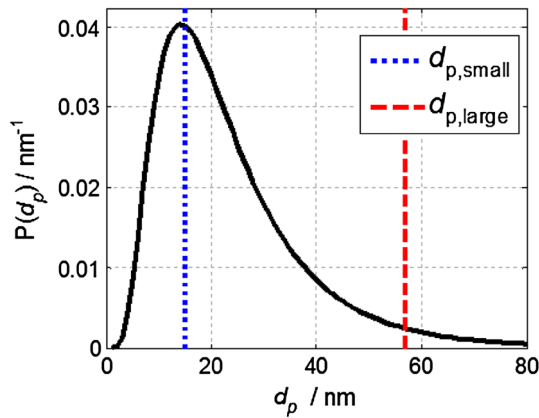
Fig. 6 Lognormal distribution function of particle sizes for $d_{cmd} = 20$ nm and $\sigma_g = 1.8$. The vertical lines show the monodisperse equivalent particle sizes evaluated from the exponential decays (see text) representing the small and large particle class of $d_{p,small} = 15$ nm and $d_{p,large} = 57$ nm, respectively

from the pre-exponential intensities with the TERF method. In a monodisperse soot ensemble, the LII signal is linearly proportional to the soot volume fraction [21] which can be defined in terms of the primary particle diameter, and the average number of primary particles, n_p:

$$f_v = \frac{\pi}{6} n_p d_p^3 \tag{3}$$

The magnitude of the LII signal at $t = 0$ for the small and large particle-size classes where all particles are at the same temperature (at least for atmospheric or sub-atmospheric pressure, see [5]) is given in Fig. 5a by the ratio of the LII-signal intensities, $S_{LII}(0)$, at the time of the laser pulse ($t = 0$ s):

$$\frac{S_{LII,small}}{S_{LII,large}} = \frac{n_{p,small}}{n_{p,large}} \frac{d_{p,small}^3}{d_{p,large}^3} \tag{4}$$

The ratio of number densities $n_{p,small}/n_{p,large}$ (denoted with R_n hereafter) is calculated as 12.9. The actual ratio

for the identical $d_{p,small}$ and $d_{p,large}$ is 14.4 over the assumed lognormal distribution curve.

Because the particle-size distribution is a continuous function, the diminishing contribution of the small particles to the overall signal also continuously decreases with time. Therefore, there is not a perfect delay time that can be defined to separate the range of small and large particles. To see the effect of various chosen delay times, this value is changed from 10 to 600 ns in 10-ns increments while determining $d_{p,small}$, $d_{p,large}$, and R_n (Fig. 7).

As the delay time increases, the contribution of the small particles to the signal segment after the delay gradually decreases, and the lifetime of this signal segment increases resulting in evaluation of larger particles. Similarly, when the delay time increases, the difference curve representing the cooling of the small particles contains a larger contribution from larger particle classes, and consequently, the evaluated particle size increases (Fig. 7a). However, an optimum delay time range exists for this strategy. When the delay time is too short, the latter segment used for the exponential fit contains too much information from the different size classes leading to a severe reduction of the fitting accuracy. Likewise, with a too large delay, the weight of larger particles in the difference curve increases and the evaluated $d_{p,small}$ does not represent an accurate mean size for the smallest size classes. The R_n curves in Fig. 7b also support this argument: For too early or too late delay times, the predicted results with the TERF method deviate from the actual R_n that is evaluated from the original distribution. For the present conditions, a delay time at around 200 ns gives a ratio close to the actual distribution. This optimum delay may vary for different distributions (this will be further analyzed in Sect. 4.2).

2.4 Evaluation of various particle-size distributions

The strategy described before was tested on polydisperse soot ensembles with various distribution characteristics. In addition to the wide lognormal distribution introduced in Sect. 2.3, a narrower lognormal distribution and two

Fig. 7 **a** $d_{p,small}$ and $d_{p,large}$ and **b** ratio of the number densities as a function of the chosen delay time
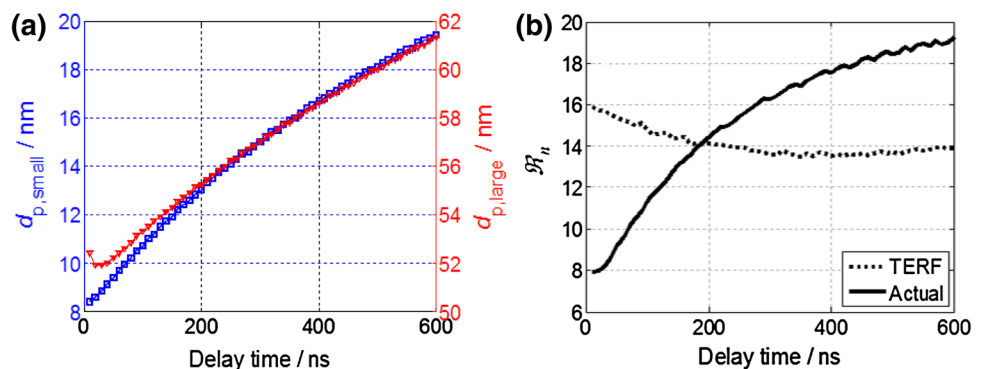
Table 2 Parameters of the investigated particle-size distributions

Parameters	a	b	c
Distribution	Lognormal	Bimodal	Bimodal
$d_{cmd,1}$ (nm)	15	15	15
$\sigma_{g,1}$	1.5	1.4	2
w_1	1	3	1
$d_{cmd,2}$ (nm)	–	40	30
$\sigma_{g,2}$	–	1.3	1.5
w_2	–	1	1

bimodal distributions with distinctive shapes were analyzed. The bimodal distribution functions, $p_{bimodal}$, were created from two standard lognormal distributions superimposed with independent weight functions [11]:

$$p_{bimodal} = w_1 p_1 (d_{cmd,1}, \sigma_{g,1}) + w_2 p_2 (d_{cmd,2}, \sigma_{g,2}) \qquad (5)$$

p_1 and p_2 are the probability density functions with lognormal distributions, whereas w_1 and w_2 are the weight factors for the small-size mode and the large-size mode, respectively. The distribution parameters used in this section are listed in Table 2.

The distribution functions are shown in Fig. 8 (each data point on the distribution curves represents the probability density of a 1-nm-wide bin) along with the evaluated small and large monodisperse equivalent mean particle sizes (vertical lines). For all the three cases, the delay time was 220 ns. The actual R_n calculated from the distribution function (ratio of $P(d_p)$ at $d_{p,small}$ and $d_{p,large}$) and the R_n calculated with the TERF method are given on the respective plots.

In all three cases, the evaluated $d_{p,small}$ and $d_{p,large}$ fall within the distribution and represent a mean particle size within their size classes. The R_n values evaluated with the TERF method also show good agreement with the actual R_n derived from the probability density functions at $d_{p,small}$ and $d_{p,large}$.

3 Experiment

Particle-size measurements were taken in a non-premixed ethylene/air Santoro flame [22] operated under standard conditions (C_2H_4: 0.232 standard liters per minute (slm), air co-flow: 43 slm). To stabilize the flame, a chimney with a 25-cm diameter was mounted 30 cm above the burner. The schematics of the experiment are shown in Fig. 9. For LII, the fundamental of a Nd/YAG laser at 1,064 nm was used with a pulse width of 7 ns. A set of cylindrical lenses forms a horizontal laser sheet, and a 1-mm slit aperture crops the laser sheet into a rectangular shape that is relay-imaged into the center of the flame with a spherical lens
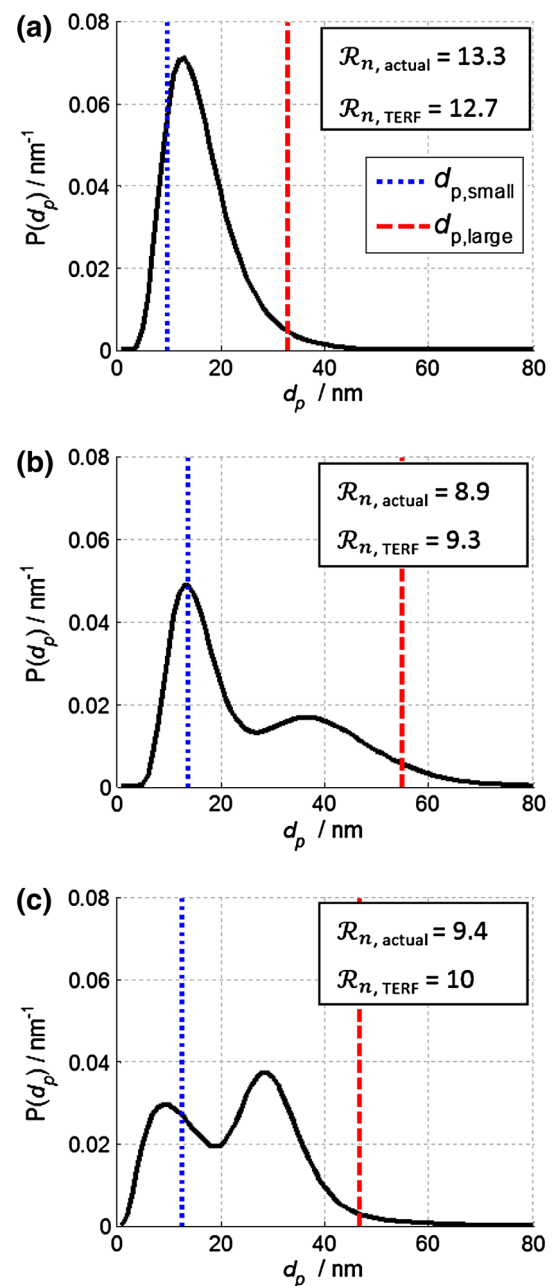
Fig. 8 Probability density functions for lognormal (**a**) and bimodal (**b**, **c**) distributions. *Vertical lines* show the monodisperse equivalent particle sizes evaluated for the small and large particle classes

at a 2f distance creating a nearly top-hat intensity profile. This spatial profile was measured with a beam profiler. The laser fluence was set to 0.08 J/cm^2 which does not cause any considerable soot evaporation. The LII signal was detected with a fast photomultiplier (PMT, Hamamatsu R7400U-04, rise time ~0.78 ns) coupled with a band-pass filter (425 ± 15 or 676 ± 14 nm) and stored on a 1-GHz oscilloscope. The photomultiplier was combined with a system of two spherical lenses and a circular aperture to
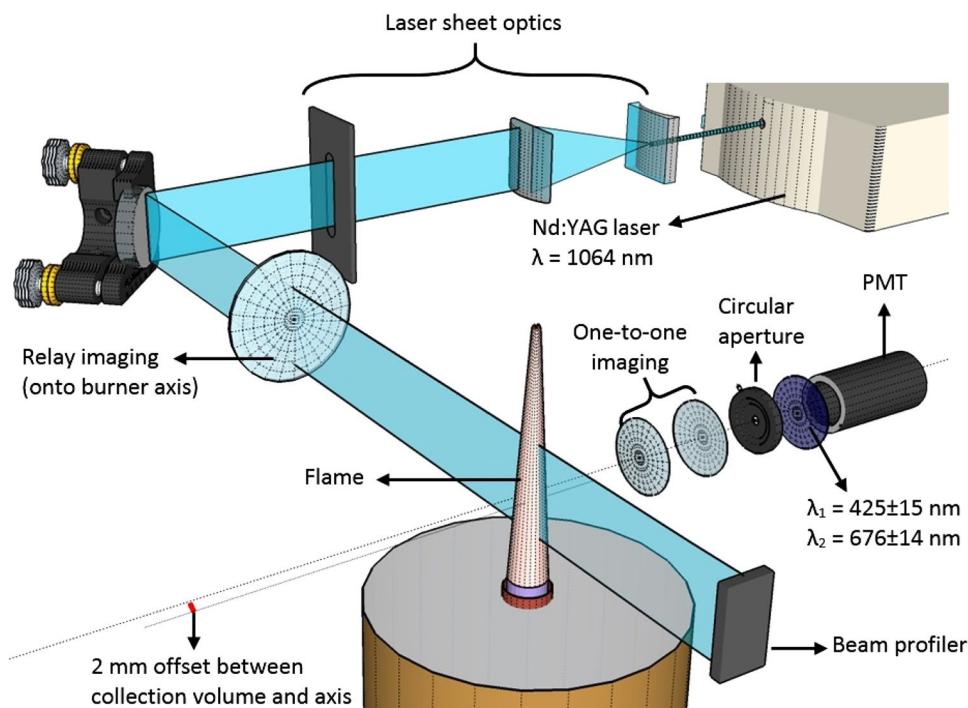
provide high spatial resolution. This collection volume (circular probe zone) in the flame has a diameter of 1.5 mm, and it was located at a 2-mm distance to the burner axis on the pump laser entrance side. This radial location has a higher soot mass with respect to the burner axis location; thus, better signal-to-noise ratios can be achieved. The burner and the chimney were mounted on a vertical translation stage independent from the optical path, which enables different heights in the flame to be probed.

The measured LII decay curves were recorded at heights between 30–70 mm above the burner (HAB) in steps of 5 mm. At each location, 100 single measurements were taken with each of the two band-pass filters. Prior to the LII measurements, the detection system was spectrally calibrated by replacing the burner with a broad-band halogen lamp with known irradiance.

For ex situ characterization, thermophoretic sampling was achieved at five HAB positions using a pneumatically driven soot sampling probe on which lacey carbon-coated copper grids were attached. The probe consisted of two thin metallic plates in a sandwich form, with a 3-mm-diameter hole exposing both sides of the TEM grid to the flame (a similar design is shown in Ref. [23]). The purpose of using a lacey grid was to minimize the distortion of the electron beam by the carbon film during the microscope imaging. A high-frame-rate camera (1,000 fps) positioned perpendicular to the pneumatic cylinder axis was mounted to measure the probe trajectory and the timing precisely. The exposure time of the probe to the flame environment (time duration where the grid rests within the flame) was set to 40 ms,

whereas the transit time (where the grid moves within the flame boundary) was shorter than 3 ms. Additional samples were collected with 60 and 80 ms exposure times at 50 mm HAB to analyze the effect of exposure time on soot sampling. The radial distance of the grid center was 2 mm from the burner axis. The sampled soot was analyzed with a Tecnai FEG 200-kV transmission electron microscope, images were recorded at 26,000× magnification, and micrographs were manually analyzed using the freeware ImageJ. It should be noted that the TEM analysis of grids in this work was conducted by a third party TEM operator who had no extensive experience in soot research. The operator acquired ~40 images from each grid, and it is lately understood that in each of these images, large aggregates were targeted and all the possible isolated particles and small aggregates were omitted. Therefore, the TEM-derived results in this work do not represent the entire soot ensemble in the respective sampling location.

4 Results and discussion

4.1 Input parameters

At each probe volume along the flame, the ambient conditions must be known for accurately modeling the LII heating and cooling processes that may vary due to radiative cooling, changing mixture fraction, and changing soot morphology. In this study, the heat-up temperature of the laser-heated soot particles was derived via pyrometry from

the ratio of peak LII-signal intensities within two detection bands by using a lookup table method [24]. These spectral bands (425 ± 15 and 676 ± 14 nm) were selected according to the recommendation of [25]. The specific emissivity values for each of these spectral bands are calculated according to Ref. [26]. A variation of the soot absorption function $E(m)$, therefore emissivity, along the flame height was not considered in this work, and identical values were used at all locations. To suppress the influence of background signal, i.e., line-of-sight-integrated flame luminosity, the baseline signal before the laser pulse was subtracted at each location. The heated soot cross section is much thinner than the flame itself. Thus, the relative contribution of this cross section to overall line-of-sight-integrated natural soot incandescence is highly low. Furthermore, the background signal is much lower (two orders of magnitude) than the LII signal. Therefore, errors due to the subtraction of flame luminosity at the region of interest from the LII signal are negligible. To measure the effective bath gas temperature, the measurements were repeated at HAB 60 mm without the laser pulse. At around this height, the radial temperature gradients are minimal and the temperature is uniform at a radial plane [27]; thus, a biasing toward lower temperatures due to edge effects was negligible. The bath gas temperature at this height was measured with two-color pyrometry. The measured temperature for this location was also in good agreement with the thermocouple measurements in Ref. [27]. Through subtracting the bath gas temperature from the heat-up temperature, the temperature increase due to the laser light absorption was calculated as 1,650 K at this height. By assuming a constant soot absorption function $E(m)$ at all flame heights, the temperature increase was also assumed constant at all locations, and the bath gas temperatures were calculated for the flame heights, respectively. The flame- and heat-up temperatures used for simulating LII signals are shown in Table 3.

At the investigated radial location, bath gas temperatures decrease with increasing HAB due to the cooling of the flame via radiation and convection (at another radial position different trends might occur depending on air entrainment). Aggregate sizes also change with flame height [9], and the values shown in Table 3 are estimations based on TEM analysis. The other input parameters used at each location are shown in Table 1. With a rough estimation, the precision of the heat-up temperature measurement via two-color pyrometry can be taken as ± 100 K, the bath gas temperature ± 200 K and the aggregate size ± 40 particles. The influence of these uncertainties on the evaluated particle size is shown in Fig. 10. The total uncertainty of the evaluated particle size due to these input parameters is approximately ± 20 %.

For this analysis, a control LII signal for Table 1 conditions is generated. Subsequently, this simulated signal trace

Table 3 Heat-up temperature, bath gas temperature, and aggregate size input parameters imposed for particle sizing at different heights above burner (HAB)

HAB (nm)	$T_{\text{heat up}}$ (K)	T_{gas} (K)	N_p
30	3,414	1,764	40
35	3,390	1,740	50
40	3,351	1,701	60
45	3,271	1,621	70
50	3,259	1,609	80
55	3,282	1,632	90
60	3,225	1,575	80
65	3,235	1,585	70
70	3,162	1,512	60
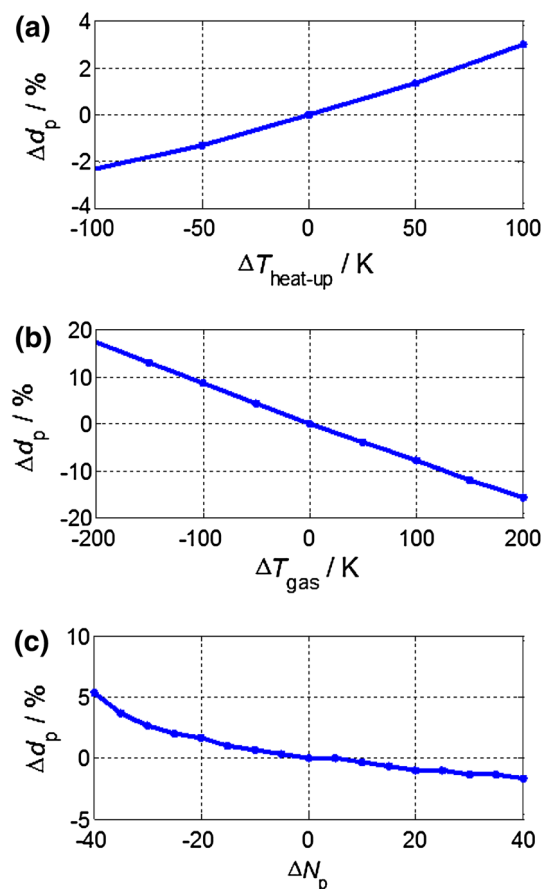
Fig. 10 Uncertainties of the particle-size determination from the TiRe-LII-signal traces due to variations in the underlying heat-up temperature (**a**), bath gas temperature (**b**), and aggregate size (**c**) compared to Table 1 conditions

is fitted by the LII model. Using this signal and the identical boundary conditions as input for the curve-fitting procedure, the original 30 nm size is reproduced. To understand how the particle-size evaluation is influenced by incorrect
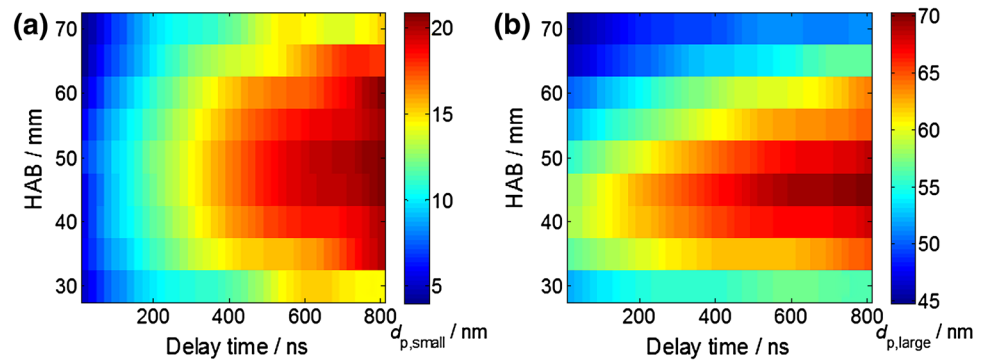
assumptions of the heat-up temperature, the bath gas temperature, and the aggregate size, the assumed values for the relevant input parameters are systematically changed within a given range (one by one). The sensitivity of the system to the respective variable can be determined from the deviation in the evaluated results. The x-axis shows the nominal difference of the modified variable from the reference boundary conditions, whereas the y-axis indicates the relative change of the evaluated particle size with respect to the original diameter.

4.2 Particle sizing

Particle sizes were determined from the LII-signal traces acquired at 425 ± 15 nm. Although the blackbody spectral radiation intensity is relatively lower at the shorter detection wavelength with respect to larger detection wavelength, it gives a better performance in distinguishing the LII signal from the natural luminosity of soot (which peaks at longer wavelengths according to the respective gas temperature) at the line of sight of detection. Furthermore, the PMTs used in this work have a higher spectral response at the shorter wavelengths, thus a better signal-to-noise ratio can be achieved at 425 nm. This wavelength also captures emission from CH band at 430 nm and the C2 Swan band 438.2 nm. However, with the gain settings of PMT adjusted for LII, such emissions are negligible as the radical chemiluminescence emission is buried below the LII emission intensity. During the study, the particle sizing was repeated with signals at 676 nm (not shown here) and the results at each measurement location were in satisfactorily close agreement with those obtained at 425 nm. The TERF method introduced in Sect. 2.3 was applied for each signal trace. Additionally, the monodisperse equivalent mean particle sizes were evaluated by full signal fitting. To investigate the influence of the delay time with the TERF method, it was swept from 20 to 800 ns in 20-ns increments, and at each delay, $d_{p,small}$ and $d_{p,large}$ were calculated (Fig. 11). Similar to the model-based analysis results, $d_{p,small}$ and $d_{p,large}$ increases with increasing delay time due to the
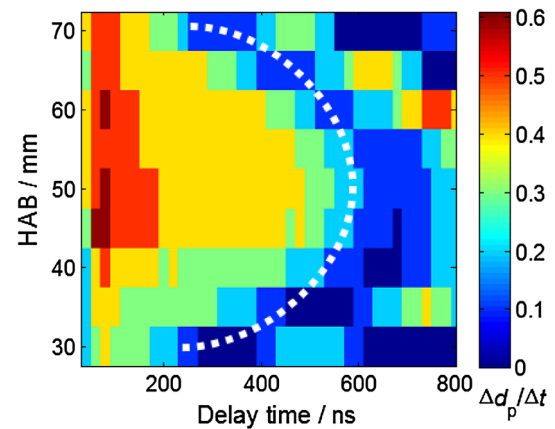

Fig. 12 Derivative of the particle sizes at each HAB with respect to changing delay time

increasing contribution of larger particles in the respective input signal segments.

As described in Sect. 2.3, the optimum delay time for each signal depends on the actual particle-size distribution. In an ideal case, the evaluated particle size should be least sensitive to changing delay time at around its optimum as it ensures that information blending from different particle size classes is minimal. To define these optimum points, a derivative of the particle sizes (large mode) at each HAB was taken with respect to the changing delay time as shown in Fig. 12. The strong oscillations in the derivative results (for fixed HAB) were filtered out with a median filter. The optimum delay time is defined as the point where $\Delta d_p/\Delta t$ first approaches 0.1 nm/ns and is marked with a white dashed line (parabola). The optimum delay time is as low as 240 ns at zones where particles are relatively small and reaches values above 600 ns at flame locations where the largest particle diameters are expected. Any increase in $\Delta d_p/\Delta t$ after this optimum delay can be attributed to noise in the acquired data.

By using these optimum delay times, R_n at each HAB is calculated and shown in Fig. 13 with the respective $d_{p,small}$ and $d_{p,large}$. The monodisperse equivalent particle

Fig. 13 $d_{p,small}$, $d_{p,large}$ and relative ratio of number densities calculated with the respective optimum delays (cf. Fig. 12) as a function of HAB. $d_{p,mono}$ is evaluated with full curve fitting
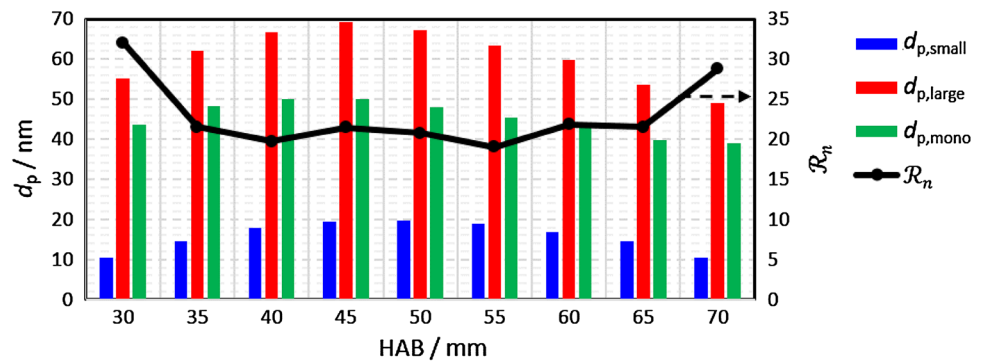
size $d_{p,mono}$ is also shown. For all size classes, the particle diameter increases with the flame height and reaches a maximum at 50 mm HAB for the small mode and at 45 mm HAB for the large mode and the monodisperse equivalent size. After these peak points, particle diameters gradually decrease indicating that soot particle sizes are affected by increasing oxidation. Within the flame height domain between 30 and 70 mm HAB, the deviation in particle size is ~10 nm for the small mode and the monodisperse equivalent mean size, whereas it is more than 20 nm for the large mode.

Figure 13 also shows that R$_n$ has an inverse relation with particle sizes. In soot formation and oxidation zones, the population of small particles with respect to larger ones is greater and reaches its minimum within the zone where the largest particle diameters are evaluated (soot oxidation and soot formation are in balance). This trend of R$_n$ is directly related to different rates of changes in particle size classes. The relative difference of $d_{p,small}$ and $d_{p,large}$ with respect to $d_{p,mono}$ at each flame height shows that the small particles are generally much smaller than the mean particle size in the formation and oxidation zones. This gap reaches its minimum around in the zone where formation and oxidation is balanced, whereas the difference between large particles and mean particle size reaches its maximum in the zone.

### 4.3 Comparison of LII and TEM particle sizing

The soot-particle size was additionally determined from TEM micrographs acquired at five HAB ranging from 30 to 70 mm (40 ms grid exposure time). For each position, the obtained primary particle diameters were divided into size bins and represented as a histogram. The histograms were then fitted by lognormal particle-size distributions to obtain continuous distribution functions. A lognormal distribution fits the particle sizes well for all locations (Fig. 14a). The total number of samples N_{TEM} counted as a function of HAB is given in each graph. The $d_{p,small}$ and $d_{p,large}$ values obtained from the TERF-derived LII-signal

analysis for the same locations are also plotted as blue and red dashed vertical lines, respectively, and $d_{p,mono}$ values obtained by full curve fitting are shown with green dash-dotted vertical lines. The TEM measurements yielded a similar trend of particle size change as the LII measurements along the flame height. The mean particle size reaches a maximum at 40 mm HAB and then gradually decreases due to oxidation.

In most of the locations, $d_{p,large}$ obtained by LII falls within the particle-size distribution derived from TEM measurements, particularly within the large particle classes. On the other hand, $d_{p,small}$ is smaller than the smallest particles measured from TEM for all cases. The main reason for this difference is attributed to the strong bias in evaluating TEM images. Usually, the small particles are either isolated or they exist as small aggregates which reduces the probability of their collision to the lacey carbon film used here (cf. Fig. 14b). Furthermore, as mentioned in Sect. 3, the TEM operator was prone to capturing large aggregates as they provide more information for the statistical analysis of primary particle size measurements (on each grid, ~40 images were taken) and mostly ignored isolated particles. Structures of soot aggregates can also be problematic for the measurement of small particles. Identifying the smaller particles at the center of an aggregate is hindered due to the relatively larger optical density of large particles that cover the small ones. Additionally, even with a small degree of bridging [28] between small and large particles, it becomes more difficult to perceive the spherical structure of small particles and a diameter cannot be measured successfully. Such bridging of small particles was mostly observed at the periphery of the aggregates, and two examples are shown in Fig. 14c. These images also indicate that initially loosely connected small individual particles that give rise to rapidly cooling LII signal might get fused to the larger particles in the supporting agglomerate during sampling and aging in between sampling and TEM measurements. Therefore, the statistical relevance of the TEM-derived number of particles with small diameters may be biased. All these observations indicate that large numbers of very small particles

Fig. 14 a Classification of primary particle sizes from TEM (*gray bars*) with lognormal fits (*black lines*) obtained from soot at five HAB from 30 to 70 mm. LII TERF-derived $d_{p,small}$ and $d_{p,large}$ values are shown as *blue dotted* and *red dashed vertical lines*, respectively, and $d_{p,mono}$ values are shown with *green dash-dotted vertical lines*. **b** Soot aggregates on a lacey carbon film. **c** Bridging of small particles with the larger ones at the aggregate periphery. Due to the lost perception of sphericity, a measurement of diameter is not possible for such particles, and therefore, they are systematically not included in the statistical analysis. Even smaller particles that might have existed on the agglomerate surface might have got fused entirely with the surface layer and therefore remain invisible
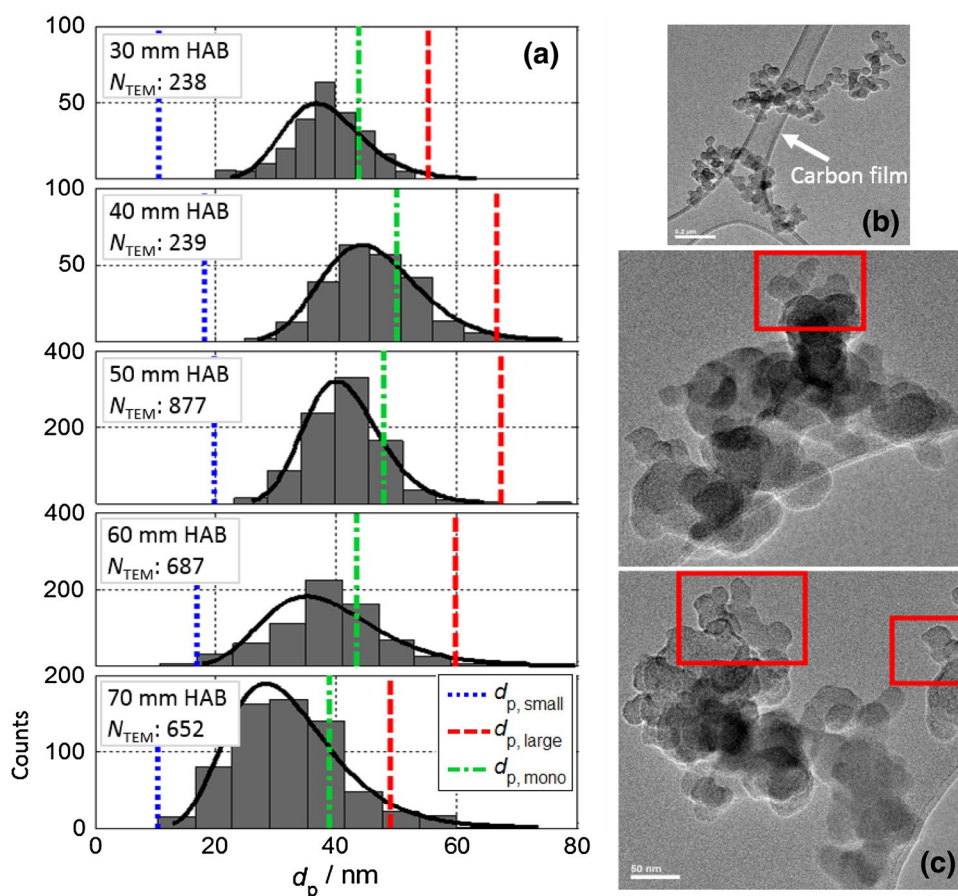
might be systematically overlooked when investigating TEM images of polydisperse soot samples.

Another reason for the discrepancy may be the unknown thermal accommodation coefficient, α_T. Bladh et al. [9] reported that α_T depends on the soot morphology and also may decrease with increasing soot maturity (i.e., higher up in the flame). In this work, however, a constant α_T was used for all locations and all size groups. If a relatively larger α_T was used for the younger particles, i.e., smaller particles in the formation zone, a more efficient loss of energy to the surrounding atmosphere would be simulated for these particles. This would eventually lead to a faster signal decay, hence evaluation of relatively larger diameters in the small-size classes. Daun et al. [29] showed that the cooling curve of soot starts with a period of what they call "anomalous cooling" where the cooling rate is as much as a factor of 2 higher than the model predictions. This period of anomalous cooling is confined to the first 50 ns after the peak of the laser pulse and its origin has not been understood yet [30]. Such anomalously high cooling rate in the acquired signal results in smaller derived primary particle sizes and can be another source of the discrepancy between the sampling results and optical results for the small particle size classes. In TERF, the information derived for the small

particle class can potentially be affected by this effect. The large particle class, however, is not affected because its information is derived from a phase after the effects of anomalous cooling are gone. This can also be considered an advantage compare to methods that fit the entire LII decay with a multi-parameter function where the entire result can be distorted—as long as anomalous cooling cannot be covered by the LII model used.
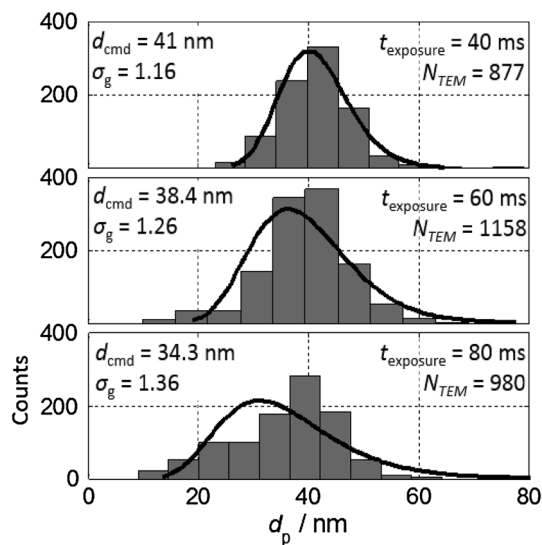
To better understand the discrepancy between the TERF-LII-derived and the TEM-derived small particle sizes, for each HAB, a phantom polydisperse TiRe-LII signal was simulated with the respective TEM distributions shown in Fig. 14a and input parameters shown in Table 3. This means that the resulting phantom signal includes no information for particles smaller than what observed in the TEM. Consecutively, $d_{p,small}$ and $d_{p,large}$ were evaluated with the TERF method. At each HAB, the evaluated $d_{p,small}$ were found to be larger than the values obtained from the experimental data, cf. Fig. 15. This indicates that the discrepancy between in situ and ex situ measurements is most likely due to the incomplete information derived from TEM.

For thermophoretic sampling, various exposure times of the grid varying from 25 to 300 ms were used in the past [9, 23, 31]. In this study, the effect of varying the exposure
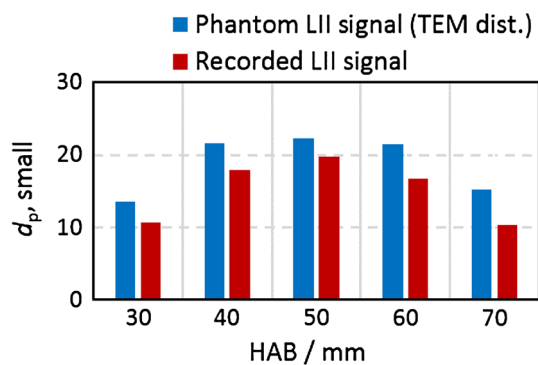
Fig. 15 $d_{p,small}$ calculated with acquired LII signal and phantom polydisperse TiRe-LII signal simulated with the respective TEM distributions. The larger $d_{p,small}$ evaluated with the phantom signal at each HAB indicates that the TEM may fail to provide correct information about the smallest particles that contribute to the LII signal

Fig. 16 Histograms of TEM-derived particle sizes with lognormal fits for soot sampled at 50 mm HAB with varying exposure times

the same time, additional particles are continuously deposited until the end of exposure time. Therefore, the width of the particle-size distribution σ_g increases with increasing exposure time and the distribution increasingly deviates from lognormal. This exposure time-dependent particle sizing result is in contrast to the conclusion drawn in Ref. [23]. Nevertheless, the sampling location in that work is not mentioned which can be the reason of the discrepancy. In fuel-rich zones, deposited particles would not oxidize. Instead, the deposited particles would be subjected to co-aggregation with the latter particles. To minimize the effects of sampling on particle sizing, the shortest exposure time should be selected that permits collecting sufficient particles for the TEM imaging.

Perturbations of the flame during sampling can cause additional uncertainty in TEM particle sizing. The high-repetition-rate movies showed that the flow induced by the moving probe severely distorts the flame. This distortion starts shortly after the probe reaches its stationary position and lasts up to 10 ms. The forced flow and the subsequent unsteadiness of the flame may cause deposition of soot on the grid that stems from locations outside the intended probe volume.

5 Conclusions

A signal-processing method, TERF, was developed for TiRe-LII in polydisperse soot that provides information about the size range and the relative weight of the small and the large fraction of the particle ensemble. The method separates the signal contribution of small and large particles from the overall signal by approximating the LII signal from size classes with narrow size distributions with monoexponential decays. A monodisperse equivalent mean particle size is then evaluated for both size classes, and the relative ratio of the number densities of both groups is determined. Compared to time-consuming polydisperse-fitting algorithms, the extracted information is limited. Nevertheless, compared to previous methods, it is not necessary to assume the shape of the distribution and the much faster evaluation makes TERF suitable for real-time analysis.

The validity of approximating LII-signal traces with monoexponential decays was analyzed with LII-signal traces simulated for monodisperse soot for various input parameters such as pressure, aggregate size, and heat-up temperature. Suitable ranges of conditions where the TERF method works reliably were determined and the error imposed by the approximation was found to be less than 2 %. High heat-up temperatures that cause strong soot evaporation was found to be the conditions where the method cannot be used. The accuracy of the method was tested on simulated signals with lognormal and bimodal

time on the TEM particle sizing was investigated by exposing the grid to the flame for 40, 60, and 80 ms. The respective particle-size histograms together with their lognormal fit are compared in Fig. 16. The corresponding d_{cmd} and σ_g values are given in each plot. A systematic decrease in the d_{cmd} and a widening of the distribution is observed with increasing exposure time. The measurements were taken at 50 mm HAB where soot oxidation dominates and deposited soot particles are exposed to excess oxygen and high temperature. Because the soot particles are only loosely attached to the thin lacey carbon coating, cooling from the supporting copper grid is not efficient. During this phase, particles eventually partially oxidize and it cannot be excluded that small particles disappear completely. At

particle-size distributions with various distribution parameters. In all cases, the method yielded satisfying results.

The TERF method was applied to measured signal traces acquired with a time-resolved detection setup at nine axial locations in a non-premixed atmospheric laminar ethylene/air flame from a Santoro burner. The LII measurements were supported by two-color pyrometry of particle heat-up temperatures. Low-fluence excitation prevented soot evaporation. A model-based analysis was performed to identify the dependence of LII particle sizing quantitatively on the assumed input parameters such as bath gas temperature, heat-up temperature, and soot morphology. At each location, a monodisperse equivalent mean particle size was also evaluated and compared to TERF method results.

For ex situ characterization, soot particles were sampled at multiple flame heights using a pneumatically driven soot sampling probe. Particle-size distributions were derived from TEM measurements and compared to the LII-derived results. It was observed that the TERF method provides sizes for the large particle class that are in good agreement with the TEM measurements. Substantial discrepancies were observed, however, between LII and TEM results for the small mode. The discrepancies were mainly associated with the biased sampling and TEM operations that omits the analysis of small-size classes. The effect of varying exposure times of the TEM grid to the flame was analyzed. At a location with excess oxygen, long exposure times cause an increased oxidation of initially deposited soot; thus, the measured mean particle size decreases and the distribution widens.

References

1. L.A. Melton, Appl. Opt. **23**, 2201–2208 (1984)
2. C. Schulz, B.F. Kock, M. Hofmann, H.A. Michelsen, S. Will, B. Bougie, R. Suntz, G.J. Smallwood, Appl. Phys. B **83**, 333–354 (2006)
3. H.A. Michelsen, F. Liu, B.F. Kock, H. Bladh, A. Boiarciuc, M. Charwath, T. Dreier, R. Hadef, M. Hofmann, J. Reimann, S. Will, P.-E. Bengtsson, H. Bockhorn, F. Foucher, K.-P. Geigle, C. Mounaïm-Rousselle, C. Schulz, R. Stirn, B. Tribalet, R. Suntz, Appl. Phys. B **87**, 503–521 (2007)
4. M. Hofmann, B.F. Kock, C. Schulz, in *Eur. Combust. Meet.*, *European Combustion Meeting 2007, Chania*, 2007
5. M. Charwath, R. Suntz, H. Bockhorn, Appl. Phys. B **104**, 427–438 (2011)
6. F. Liu, B.J. Stagg, D.R. Snelling, G.J. Smallwood, Int. J. Heat Mass Transf. **49**, 777–788 (2006)
7. M. Hofmann, B.F. Kock, T. Dreier, H. Jander, C. Schulz, Appl. Phys. B **90**, 629–639 (2007)
8. B. Menkiel, A. Donkerbroek, R. Uitz, R. Cracknell, L. Ganippa, Combust. Flame **159**, 2985–2998 (2012)
9. H. Bladh, J. Johnsson, N.-E. Olofsson, A. Bohlin, P.-E. Bengtsson, Proc. Combust. Inst. **33**, 641–648 (2011)
10. S. Banerjee, B. Menkiel, L.C. Ganippa, Appl. Phys. B **96**, 571–579 (2009)
11. J. Johnsson, H. Bladh, P.-E. Bengtsson, Appl. Phys. B **99**, 817–823 (2010)
12. A.D. Abid, N. Heinz, E.D. Tolmachoff, D.J. Phares, C.S. Campbell, H. Wang, Combust. Flame **154**, 775–788 (2008)
13. S. Dankers, A. Leipertz, Appl. Opt. **43**, 3726–3731 (2004)
14. N.A. Fuchs, Geofis. Pura E Appl. **56**, 185–193 (1963)
15. F. Liu, K.J. Daun, D.R. Snelling, G.J. Smallwood, Appl. Phys. B **83**, 355–382 (2006)
16. K.J. Daun, B.J. Stagg, F. Liu, G.J. Smallwood, D.R. Snelling, Appl. Phys. B **87**, 363–372 (2007)
17. F. Liu, G.J. Smallwood, D.R. Snelling, J Quant. Spectrosc. Radiat. Transf. **93**, 301–312 (2005)
18. M. Hofmann, *Laser-Induced Incandescence for Soot Diagnostics at High Pressure*, Ph.D. thesis, Heidelberg University, 2006
19. D.R. Snelling, G.J. Smallwood, F. Liu, Ö.L. Gülder, W.D. Bachalo, Appl. Opt. **44**, 6773–6785 (2005)
20. S. Will, S. Schraml, K. Bader, A. Leipertz, Appl. Opt. **37**, 5647–5658 (1998)
21. E. Cenker, G. Bruneaux, L.M. Pickett, C. Schulz, SAE Int. J. Engines **6**, 352–365 (2013)
22. R.J. Santoro, H.G. Semerjian, R.A. Dobbins, Combust. Flame **51**, 203–218 (1983)
23. R.A. Dobbins, C.M. Megaridis, Langmuir **3**, 254–259 (1987)
24. P.B. Kuhn, B. Ma, B.C. Connelly, M.D. Smooke, M.B. Long, Proc. Combust. Inst. **33**, 743–750 (2011)
25. F. Liu, D.R. Snelling, K.A. Thomson, G.J. Smallwood, Appl. Phys. B **96**, 623–636 (2009)
26. D.R. Snelling, F. Liu, G.J. Smallwood, Ö.L. Gülder, Combust. Flame **136**, 180–190 (2004)
27. R.J. Santoro, T.T. Yeh, J.J. Horvath, H.G. Semerjian, Combust. Sci. Technol. **53**, 89–115 (1987)
28. J. Johnsson, H. Bladh, N.-E. Olofsson, P.-E. Bengtsson, Appl. Phys. B **112**, 321–332 (2013)
29. K.J. Daun, G.J. Smallwood, F. Liu, J. Heat Transf **130**, 1–9 (2008)
30. D.R. Snelling, K.A. Thomson, F. Liu, G.J. Smallwood, Appl. Phys. B **96**, 657–669 (2009)
31. K. Tian, K.A. Thomson, F. Liu, D.R. Snelling, G.J. Smallwood, D. Wang, Combust. Flame **144**, 782–791 (2006)